Are actinyl cations good probes for structure determination in solution by NMR?

Md. Ashraful Islam, Matthieu Autillo, Clovis Poulin-Ponnelle, Christelle Tamain, Hélène Bolvin, Claude Berthon

Are Actinyl Cations good Probes for Structure Determination in Solution by NMR?

Md. Ashraful Islam,[†] Matthieu Autillo,[‡] Clovis Poulin-Ponnelle,[‡] Christelle Tamain,[‡] Hélène Bolvin,[*,†] and Claude Berthon[*,‡]

[†]*Laboratoire de Chimie et Physique Quantiques, CNRS, Université Toulouse III, 118 route de Narbonne, 31062 Toulouse, France*

[‡]*CEA, DES, ISEC, DMRC, Univ. Montpellier, Bagnols sur Cèze 30207, France*

E-mail: bolvin@irsamc.ups-tlse.fr; claude.berthon@cea.fr

Abstract

We report on NMR spectroscopy, CAS based method calculations and X-ray diffraction on An^{V} and An^{VI} complexes with a neutral and slightly flexible TEDGA ligand. After checking that pNMR shifts mainly arise from pseudo-contact interactions, pNMR shifts have been analyzed considering axial and rhombic anisotropy of the actinyl magnetic susceptibilities. Results are compared to a previous study performed on $[An^{VI}O_2]^{2+}$ complexes with dipicolinic acid (DPA). It is shown that $5f^2$ cations (Pu^{VI} and Np^{V}) make very good candidates to obtain the structure of actinyl complexes in solution by ^{1}H NMR spectroscopy as shown by the invariance of the magnetic properties to the equatorial ligands, conversely to the Np^{VI} complexes with a $5f^1$ configuration.

Introduction

The paramagnetic NMR (pNMR) chemical shifts induced by lanthanide III (Ln^{III}) cations also called Lanthanide Induced Shifts (LIS) have been widely used for decades to obtain

structural information on metal–ligand complexes in solution [1–7]. Nowadays, this application regained an important attention particularly in biological systems [8–10]. Conversely, the possibility of using NMR experiments to reach the structure of actinide complexes in solution through Actinide Induced Shifts (AIS) was never considered to our knowledge while it could provide valuable information in the nuclear fuel research [11–13] or in environmental science [14–16]. The issue with the actinide (An) cations is the sensitivity of their paramagnetic behavior to the ligand field conversely to the lanthanide series [17]. However, the ground state of the $[Pu^{VI}O_2]^{2+}$ cation is rather insensitive to the equatorial environment, with a well isolated ground doublet ($^3H_4$) separated from the first excited state by several thousand cm^{-1}, as for example in $[PuO_2(NO_3)_3]^-$, $[PuO_2(CO_3)_3]^{4-}$ and $[PuO_2(DPA)_2]^{2-}$ complexes. [18,19] On the contrary, the ground state of the $5f^1$ $[NpO_2]^{2+}$ neptunyl cation is very sensitive to the equatorial ligands, as exemplified by the two $[NpO_2(NO_3)_3]^-$ and $[NpO_2Cl_4]^{2-}$ complexes. [20–22] The paramagnetic chemical shifts of some symmetrical neptunyl and plutonyl cations were successfully described by the group of Autschbach. [18,23,24]

Herein, we report a structural investigation of $[An^{VI}O_2]^{2+}$-TEDGA (tetraethyl-diglycolamide) complexes in CD_3CN solution (see Figures 1, S2 and S3), the electronic and magnetic properties are analyzed by means of *ab initio* calculations and compared to previous results with the DPA ligand. [19] The aim is to assess the stability of the magnetic anisotropy of the actinyl cations towards the nature of the equatorial ligands. We will see that the $5f^1$ or $5f^2$ electronic configuration of the actinyl cation plays a key role in order to validate or not the use of the actinyl cations as probes for structural determinations.

In this purpose, two stoichiometries of the actinyl:TEDGA complexes were characterized and analyzed by NMR spectroscopy in our previous publication: [25] The 1:2 (cation:ligand) complex, expected to be symmetrical according to our single crystal X-ray diffraction (XRD) results and the 1:1 complex where the replacement of one TEDGA ligand by two water molecules is expected to reduce the symmetry of the first coordination sphere. These two species enable to study the rhombicity effect on the magnetic anisotropy tensor. However,

the TEDGA is a tridentate capable ligand as the DPA molecule but slightly more flexible with two ethyl chains on each amide moiety (Figure 1). Previous molecular dynamic (MD) simulations showed that in the 1:2 complexes in acetonitrile, the oxygen atom (O2) appears mainly above or below the coordination plane and not coordinated to the metallic center at the nano second scale.[25] Consequently, the 1:2 complexes may exist in solution in a dissymmetric structure with a coordination number of 5 instead of 6 as shown by single crystal X-ray diffraction (XRD). Nevertheless different representative conformations of the 1:2 complex differing by the ethyl chain orientations and coordination number were taken into account. Regarding the 1:1 complexes, MD simulations also show that the first coordination sphere of the actinyl is mainly completed by two water molecules rather than by three with a tridendate TEDGA ligand.[25]

Collected ^{1}H NMR shifts of the 1:1 and 1:2 complexes are analyzed within the dipolar approximation like in the previous study using MD simulations. Based on the conformational information drawn from MD, we focus here, on the magnetic susceptibility tensors from an *ab initio* point of view to get explanations at the electronic level. Results are compared to the magnetic anisotropy of the $[AnO_2(DPA)_2]^{2-}$ complexes.[19]

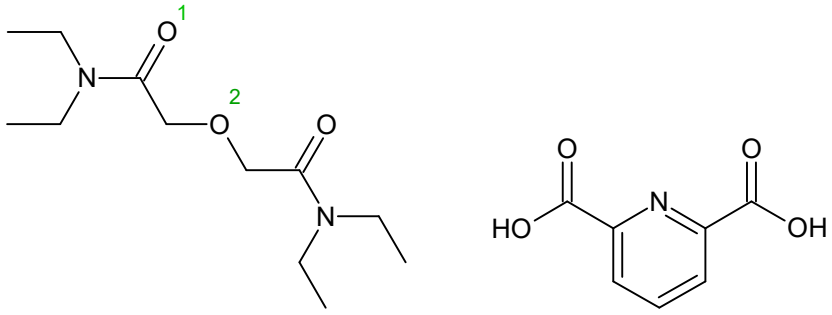

Figure 1: Comparison of TEDGA (left) and DPA (right) structures and oxygen atoms numbering on the TEDGA.

Results and discussion

Synthesis and characterization of Actinyl-TEDGA complexes

Solutions of $[An^{VI}O_2]^{2+}$ were prepared by dissolving $[(CH_3)_4N]_2An^{VI}O_2Cl_4$ compounds in CD_3CN ($[An^{VI}] \approx 0.1 mol.L^{-1}$; V = 0.5mL) (See Experimental section). Solid $AgCF_3SO_3$ was added with a molar ratio $[(CH_3)_4N]_2An^{VI}O_2Cl_4$:$AgCF_3SO_3$ of 1:4 and the resulting AgCl precipitate removed by centrifuge.

$$[(CH_3)_4N]_2An^{VI}O_2Cl_4 + 4\,AgCF_3SO_3 \xrightarrow{CD_3CN} [(CH_3)_4N]_2An^{VI}(CF_3SO_3)_4 + 4\,AgCl\downarrow$$

The Np^V solution is obtained by Np^{VI} reduction from $[(CH_3)_4N]_2An^{VI}(CF_3SO_3)_4$ in acetonitrile solution with $NaNO_2$. Successive additions of TEDGA ligand (molar ratio actinyl:TEDGA from 2:1 to 1:2) were performed directly in the freshly prepared triflate $[An^{VI}O_2]^{2+}$ and $Np^VO_2{}^+$ solutions and ^1H NMR spectra were used to follow the complexes formation. As shown Figure 2 for $[U^{VI}O_2]^{2+}$ upon consecutive additions of TEDGA in a CD_3CN solution of $[(CH_3)_4N]_2AnO_2(OTf)_4$ (OTf stands for triflate anion $CF_3SO_3{}^-$) from molar ratio R=$[An^{VI}O_2]^{2+}$:TEDGA=1 to 0.5, two sets of five signals appear successively on the ^1H NMR spectra at 252K. They are assigned to TEDGA ^1H belonging to 1:1 and 1:2 complexes respectively. The same pattern is observed at 298K proving that the TEDGA species are in slow chemical exchange at room temperature.

It was noted that the 1:1 complex (Np^V:TEDGA) is not formed in acetonitrile. The 1:2 complex is obtained by direct addition of at least 2 equivalents of TEDGA otherwise Np^V partially oxidizes to Np^{VI} for greater ratios (Np^V:TEDGA>1:2). Consequently AIS of TEDGA's ^1H were analyzed for 1:2 complexes with Np^{VI}, Pu^{VI} and Np^V and 1:1 complex with Np^{VI} and Pu^{VI}. The 1:2 and 1:1 complexes of U^{VI} complexes were used as diamagnetic references for both An^{VI} and Np^V.

The same stoichiometric species (1:1 and 1:2) are observed with $[Np^{VI}O_2]^{2+}$ and $[Pu^{VI}O_2]^{2+}$ cations. Both present ^1H spectra with negative paramagnetic chemical shifts up to -17 ppm

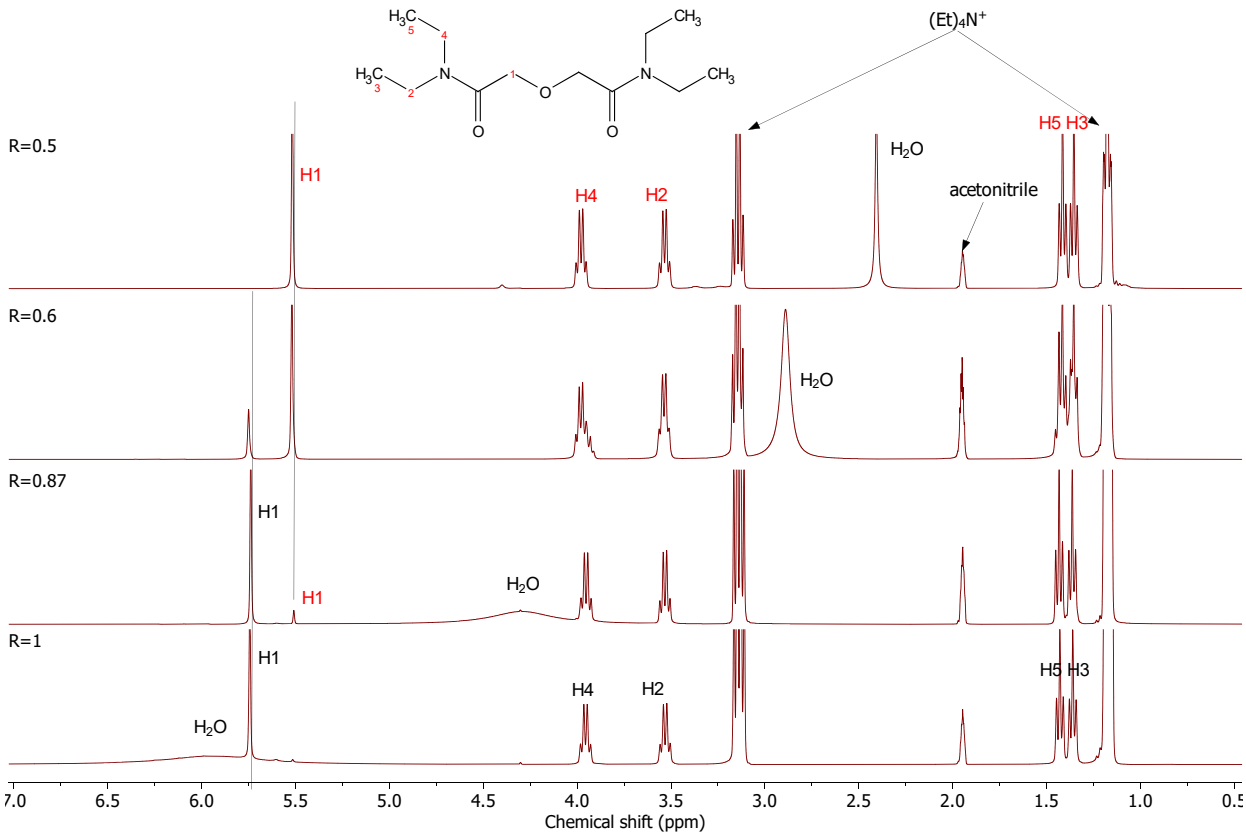

Figure 2: ^{1}H NMR spectra of $[U^{VI}O_2]^{2+}$ - TEDGA solutions in CD_3CN upon addition of TEDGA ligand at 252 K. Molar ratio R=$[U^{VI}]$:[TEDGA] from 1 to 0.5 (bottom to top spectra) with $[UO_2{}^{2+}] \approx 50\ 10^{-3}$mol.L^{-1}. ^{1}H assignments in red and black colors belong to 1:2 and 1:1 complexes respectively.

(Figures S8) and -57 ppm (Figure S9) for $[Np^{VI}O_2]^{2+}$ and $[Pu^{VI}O_2]^{2+}$ respectively. In addition, the shift and linewidth of the residual ^{1}H water signal shows that some water molecules are included in first coordination sphere of the $[An^{VI}O_2]^{2+}$ cations. This is particularly evidenced on ^{1}H NMR spectra of $[U^{VI}O_2]^{2+}$ complexes of Figure 2. For smaller molar ratio $[An^{VI}O_2]^{2+}$:TEDGA of 1:2, no additional complex was observed on the NMR spectra while ^{1}H water signal is no longer involved. This prior analysis of $[An^{VI}O_2]^{2+}$-TEDGA system strongly suggests the formation of two complexes: $[An^{VI}O_2(TEDGA)(H_2O)_x]^{2+}$ and

$[An^{VI}O_2(TEDGA)_2]^{2+}$ from the following chemical equilibria :

$$[TMA]_2An^{VI}(OTf)_4 + TEDGA \xrightleftharpoons{CD_3CN \cdot H_2O} An^{VI}(TEDGA)(H_2O)_x(OTf)_2 + 2\,[TMA](OTf)$$
$$An^{VI}(TEDGA)(H_2O)_x(OTf)_2 + TEDGA \xrightleftharpoons{CD_3CN \cdot H_2O} An^{VI}(TEDGA)_2(OTf)_2 \quad (1)$$

where OTf and TMA stand for triflate anion $CF_3SO_3^-$ and tetramethylammonium cation $[(CH_3)_4N]^+$ respectively.

The hydrogen atoms of the TEDGA were labeled according to Figure 1. Assignments are performed owing to 2D spectra for U^{VI} and Np^{VI} (Figures S11, S12 respectively). Regarding Np^V and Pu^{VI} complexes ^1H assignments were done through peak integration because ^1H relaxation is too fast compared to $1/^3J_{HH}$ to observe cross peaks on 2D NMR experiments. ^1H chemical shifts observed for $An^{VI}O_2(TEDGA)_2{}^{2+}$ (An=U, Np and Pu) and $Np^VO_2(TEDGA)_2{}^+$) with temperature are collected Tables S10, S12, S14 and S15 respectively. ^1H chemical shifts observed for $U^{VI}O_2(TEDGA)(H_2O)_x{}^{2+}$ and $Pu^VO_2(TEDGA)(H_2O)_x{}^{2+}$ with temperature are collected Tables S16 and S18 respectively.

Crystals suitable for single crystal X-ray diffraction (SC-XRD) were obtained by volume reduction of organic solutions (V=0.1mL) followed by slow crystallization with diisopropyl ether vapor diffusion. Isolated crystals were identified as $An^{VI}O_2(TEDGA)_2(CF_3SO_3)_2$ with An=U (A), Np (B), and Pu (C). See Table S1 for crystallographic details.

The Np^V complex of the TEDGA has been accidentally obtained while trying the $Np^{VI}O_2(TEDGA)_2(NO_3)_2$ synthesis. Indeed, addition of $Np^{VI}(NO_3)_2$ (brought to dryness after oxidation and Ag^+ removing with chloride) in acetonitrile with a stoichiometric amount (1:2) of TEDGA leads to a complexation of the ligand and a simultaneous Np^{VI} reduction to Np^V. After a slow crystallization, isolated crystals reveal a monoclinic structure of Np^VO_2. Because of the $[U^{VI}O_2]^{2+}$ oxidation state stability, two other nitrate compounds of the TEDGA complexes were easily obtained and analyzed by XRD : $U^{VI}O_2(TEDGA)_2(NO_3)_2$

and $[U^{VI}O_2(TEDGA)(NO_3)_2](HCCl_3)$. Noted (E) and (F) respectively they are reported in details in Table S2.

From uranium to plutonium (A to C), the An=O bond distances decrease from 1.77(1) Å to 1.74(7) Å as shown in Table 1 in agreement with the ionic radii contraction along the actinide series, while the equatorial plane An−O1/O2 (O1 and O2 are carbonyl and ethoxy oxygen atoms respectively) bond distances are less actinide dependent. For both $[U^{VI}O_2(TEDGA)_2]^{2+}$ complexes A and E, we can note the U=O bond distances are similar but a shortening and lengthening of the U−O1 and U−O2 bond distances of about 0.023Å respectively occur by replacing triflates charge compensation by nitrates. This change in uranyl first coordination sphere characterizes the flexibility of the TEDGA ligand. A larger shortening and lengthening of the U−O1 and U−O2 bond distances of about 0.1Å respectively is also observed when changing the cation charge from Np^{VI} to Np^{V} complexes (B and D respectively Table 1). The TEDGA ligands in the equatorial plane are perpendicular to the $[An^{VI}O_2]^{2+}$ moiety and keep their planar conformation. The ethyl chains of the two ligands in front of each other point in the opposite direction and minimize the ligand tilt as revealed by ∠ O=An−O1 and ∠ O=An−O2 angles close to 90°. The linearity of the central uranyl moiety and the planarity of the TEDGA ligand are greatly disturbed due to the crystal packing. In the $U^{VI}O_2(TEDGA)(NO_3)_2$ complex, the two ethyl chains further minimize repulsion by orientating themselves in the opposite face of the coordination plane.

Geometric structure of the complexes

In the study of the An^{VI}-DPA complexes, the geometry of the complexes used for pNMR shift calculations were taken from XRD results.[19] In the present study, the TEDGA is a flexible ligand and structures deduced from solid state owing to X-Ray spectroscopy may not be representative of the different conformations present in the acetonitrile solution. Furthermore the TEDGA complexes may adopt several conformations in solutions that could be in fast

Table 1: Selected bond distances (in Å) and angles (in °) from XRD spectroscopy and DFT geometry optimization of the TEDGA complexes. O1 and O2 are carbonyl and ethoxy oxygen atoms respectively (see Fig. 1).

Compound	An=O	An-O1	An-O2	∠O=An=O	∠ O=An-O1	∠ O=An-O2
			XRD			
$[U^{VI}O_2(TEDGA)_2](CF_3SO_3)_2$ (A)	1.77(1)	2.44(1)	2.62(5)	179.9(9)	89.1(6)	90.21(5)
$[Np^{VI}O_2(TEDGA)_2](CF_3SO_3)_2$ (B)	1.75(3)	2.44(6)	2.61(8)	179.9(9)	89.1(1)	91.77(4)
$[Pu^{VI}O_2(TEDGA)_2](CF_3SO_3)_2$ (C)	1.74(7)	2.43(1)	2.61(4)	180.0(0)	89.1(1)	91.8(8)
$Np^{V}O_2(TEDGA)_2(NO_3)$ (D)	1.82(2)	2.51(1)	2.71(4)	178.5(7)	89.2(2)	94.5(8)
$U^{VI}O_2(TEDGA)_2(NO_3)_2$ (E)	1.76(9)	2.42(7)	2.64(7)	179.9(9)	89.1(8)	93.2(3)
$U^{VI}O_2(TEDGA)(NO_3)_2$ (F)	1.76(4)	2.39(5)	2.59(6)	174.1(0)	86.0(5)	101.9(8)
			DFT			
$[U^{VI}O_2(TEDGA)_2]^{2+}$ 6c(TTT)	1.75	2.43	2.76	180	89.5	88.8
$[U^{VI}O_2(TEDGA)_2]^{2+}$ 6c(CCC)	1.75	2.43	2.73	177.3	88.8	90-76
$[U^{VI}O_2(TEDGA)_2]^{2+}$ 5c(TTT)	1.75	2.41-2.35	2.63-3.50	177.7	88.5	87.7-61.8
$[U^{VI}O_2(TEDGA)(H_2O)_2]^{2+}$ 5c(T)	1.75	2.37	2.62	179.2	89.7	89.6
$[Pa^{V}O_2(TEDGA)_2]^{+}$ 6c(TTT)	1.84	2.56	2.83	180	89.0	84
$[Pa^{V}O_2(TEDGA)_2]^{+}$ 5c(TTT)	1.84	2.55-2.51	2.78-3.93	178	89	89.7-66.9

chemical exchange and lead to observed pNMR chemical shifts resulting from an average of these TEDGA conformations. In the case of the 1:2 complex, the MD study revealed all the possible conformations that can be found in solution through two different modes of coordination in the equatorial plane of the cation.[25] MD simulations were in agreement with EXAFS results. The different structures differ by the number of oxygen atoms in the first coordination sphere of the actinide cation, five or six. In the six coordination mode (denoted 6c), the TEDGA ligands are planar, with only the four terminal methyl groups out of the plane and the six oxygen atoms are coordinated forming a slightly deformed hexagon. In the five coordination mode (denoted 5c), one of the TEDGA is distorted, the central oxygen atom being out of the equatorial plane with a distance of 3.8 Å, only five oxygen atoms are bonded to the An cation. The lifetimes of the 6c and 5c structures are about 3.2 and 33.5 ps respectively, showing a very fast inversion between both structures. Since these lifetimes are very short for an NMR time scale, observed NMR spectra result from an average of both coordination modes. Similarly, the experimental EXAFS signal of the $[U^{VI}O_2(TEDGA)_2]^{2+}$ corresponds to an averaged signal from the 5c and 6c structures deduced from the MD

simulations.[25]

Furthermore, the two ethyl groups on the same amide might be either on the same side of the plane (denoted C=cis), or on the opposite side of the plane (denoted T=trans) (θ_{intra}, in blue in Figure S7) and the adjacent ethyl groups from two different TEDGA ligands might be as well either C or T (θ_{inter}, in red in Figure S7). We denote the different conformers according to those angles; as an example 6c(TTC) denotes the 6 coordinated structure, with an intra T conformation on one side, a T inter conformation between the two ligands, and a C intra conformation on the other side. As an example, 5c(TTT) and 6c(CCC) conformations are presented in Figure 3.

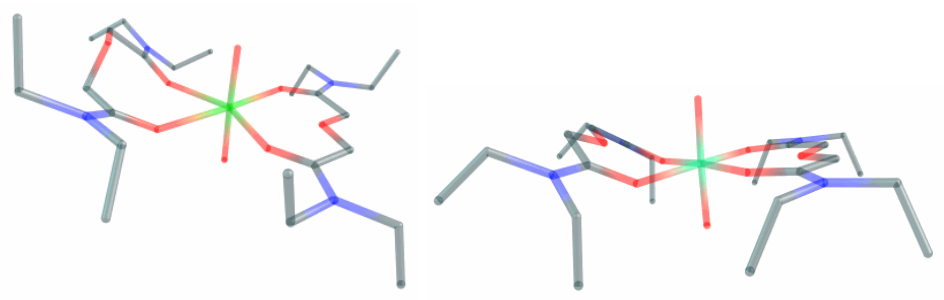

Figure 3: $[U^{VI}O_2(TEDGA)_2]^{2+}$ complex in conformation 5c(TTT) (left) and 6c(CCC) (right). Protons are removed for clarity.

More details are given in Section S1.3 of the SI. Figure S7 shows a strong variability of the dihedral angle values confirming the flexibility of the complex. Indeed, there are many different conformations for each structure.

Furthermore, MD simulations show that the intra and inter conformations are independent and that the intra T conformation is the most probable by 77% and the inter C is the most probable by 58 % (see Eq.(S1)). Those different conformers were found to be local minima of the potential energy surface using DFT geometry optimization with the B3LYP functional (Table 2). All those minima are rather close in energy, within a 15 kJ.mol^{-1} window, the lowest being the 6c(TTT) conformer. The optimized structures are compared to the XRD ones in Table 1. The bond lengths are in very good agreement, both for An^{VI} and An^{V} complexes. In all cases, the carbonyl O1 atom lies in the equatorial plane. While

the 6c(TTT) conformer is fully symmetrical, there is small distorsion of one of the TEDGA ligand in the 6c(CCC) structure. In the 5c(TTT) conformer, the non distorted TEDGA is closer to the metal ion while the bonding O2 atoms of the distorted TEDGA come even closer, the An-O2 distance confirms that the ethoxy O2 is non-bonding.

It appears clearly from this discussion, that the conformation of the $[An^{VI}O_2(TEDGA)_2]^{2+}$ complexes in solution is not clearly defined and is probably a mixture of conformers. In order to simplify the discussion with this flexible TEDGA ligand, we focused on three representative conformers, the 6c(TTT), 6c(CCC) that have the lowest and highest energy for the 6c structure respectively and the 5c(TTT) in order to take into account the different coordination modes in solution. (see Figure S2).

Table 2: Population (in %) of the 5c and 6c binding modes for $[An^{V/VI}O_2(TEDGA)_2]^{+/2+}$ complexes (with An=Np, Pu) and for each binding mode, population of the different conformers from MD simulations (from reference[25]) and deduced from Eq.(S1) with $p_T^{inter} = 42\%$ and p_T^{intra}=77% and ΔE energy differences (in kJ.mol^{-1}) from B3LYP calculations for $[U^{VI}O_2(TEDGA)_2]^{2+}$ complex in acetonitrile.

		Np^{VI};Pu^{VI};Np^{V}	TTT	TTC	CTC	TCT	CCT	CCC
population	5c	67%;82%;20%	26	14	2	36	19	3
	6c	33%;18%;80%	27	12	3	35	18	5
	Eq. (S1)		25	15	2	34	21	3
ΔE	6c		0	-	11	1	6	12
	5c		8	13	-	-	-	-

Regarding the 1:1 complexes from U^{VI} to Pu^{VI}, MD simulations show that two water molecules are in the first coordination sphere with the ether and two amide oxygens of the TEDGA coordinated (conformation noted 2W).[25] Aside this 5c structure, another complex with a third water molecule but only two amide oxygens in the first coordination sphere was observed by MD simulations (conformation noted 3W). This complex was found inconsistent with the experimental paramagnetic shifts.[25] Surprisingly, this complex with three water molecules is slightly more stable according to our DFT calculations than the 2W con-

formation (11kJ/mol difference). Since this energy difference is rather low, only the 2W conformation with Trans ethyl groups is taken into account and noted 5c(T) hereafter. The EXAFS signal on the $[U^{VI}O_2TEDGA(H_2O)_x]^{2+}$ complex confirmed this statement.[25] It has to be mentioned that geometry optimization performed by DFT on $[U^{VI}O_2TEDGA(H_2O)_3]^{2+}$ with a coordination number 6 (6c) led to a strong distortion of the first coordination sphere and a loss of one water molecule.

Ab initio electronic structures

The multiconfigurational SO-CAS/RAS based method had been successfully used to describe the electronic structures and magnetic properties of actinyl complexes.[18,19,22] In the central actinyl moiety, three of the $5f$ orbitals ($5f_\sigma$ and $5f_\pi$) are engaged in the triple bond with the two oxo groups, and are antibonding. The $5f_\delta$ and $5f_\phi$ orbitals are non-bonding in the free actinyl and host the unpaired electrons. The ordering and the composition of those latter orbitals are determined by the nature and more specifically, the symmetry of the equatorial ligands. In the case of a $5f^1$ configuration, the magnetic anisotropy is finely tuned by the equatorial ligand field, from prolate to oblate, according to the composition of the singly occupied spinor in the ground Kramers doublet.[19,22] The second Kramers doublet is usually thermally populated at room temperature and contributes largely to the magnetic properties. One usually needs to go beyond the CASSCF level for a correct description, even qualitative. It can be achieved variationnaly, by including the bonding and antibonding σ and π orbitals of the actinyl in the active space, and perturbationnally. The energy of the complexes with configuration $5f^1$ are given in Tables S20 and S21, without and with spin-orbit coupling, respectively. In all cases, the lowest spin-free states are of Δ parentage, with a splitting of some hundreds of cm^{-1}. The states with Φ parentage are between 2000 and 4000 cm^{-1} above the ground state, the splitting of the Φ state is the largest, in the 6c conformation, about 2000 cm^{-1}, because of the 6-fold symmetry of the equatorial ligands (cf Figures S2). In the the 5c and 1:1 complexes (cf Figures S2 and S3), this splitting is only about 1000 cm^{-1}, and as a

consequence, the first Φ states has a larger gap. With spin-orbit coupling, for all complexes, the inclusion of dynamical correlation switches the two lowest states. With correlation, one eventually gets the state of $M_J = \pm 5/2$ parentage as the ground states, which is a mixture of Δ and Φ states and the $\Delta_{3/2}$ states with an energy gap of some hundreds of cm^{-1}. In the 6c complexes, this gap is larger than 600 cm^{-1} and is not populated at room temperature. For the 5c and 1:1 complexes, this gap is between 400 and 500 cm^{-1} and partially populated. The composition of the Kramers doublets in terms of Δ and Φ as well as the g factors are given in Table S22. For the 6c 1:2 and the 1:1 complexes, at RASPT2 level, the composition of the ground KD is 30 % Φ and 70 % Δ leading to an axial g tensor while for the 5c complex, the ratio is 50-50 and the g tensor less axial.

The energies of the conformers calculated with the different methods are compared in Table S23. All methods predict the 6c conformer to be the most stable. The energy of the 5c conformer is much larger with CAS based methods and the energy of the two considered 6c conformers are lower than the 5c, while with B3LYP, the 5c(TTT) is lower than the 6c(CCC). With those methods, the inclusion of spin-orbit coupling does not impact those energy differences. The inclusion of dynamical effects with PT2 reverses the order of the ground configuration, the 6c(CCC) being the lowest with PT2.

On the other hand, actinyl cations with a $5f^2$ configuration are much less sensitive to the equatorial ligands. One of the unpaired electron lies in a $5f_\phi$ and the other in a $5f_\delta$ in order to minimize the electron-electron repulsion, leading to a non-Kramers doublet close to the ^4H state of the free actinyl.[18,19] The energies of the complexes with $5f^2$ configuration are given in Table S26. As usually the case, the ground state is a non-Kramers doublet essentially issued from the ^4H spin-free state (see Table S28 and Section S4.2). There is a small energy gap in the non-Kramers doublet, slightly larger in the 1:2 complex.

Paramagnetic NMR shifts and structural determination analysis

The presence of a paramagnetic center induces on the NMR spectrum of an atom K situated on the ligand an additional shift δ_K^p with respect to a diamagnetic analog. This shift is decomposed as the sum of two terms δ_K^{pc} and δ_K^c, the pseudocontact (dipolar) and the Fermi-contact components, respectively. We showed in a previous study on the $[An^{VI}O_2(DPA)_2]^{2-}$ series,[19] that the ^{1}H paramagnetic chemical shifts are dominated by the pseudocontact contribution. The pseudocontact shift δ_K^{pc} arises from the through-space magnetic dipolar interaction between the nuclear spin of the NMR active nucleus and the electronic magnetic moment of the paramagnetic center and can be expressed in ppm unit as[26]

$$\delta_K^{pc} = \frac{10^6}{12\pi N_A}(\Delta\chi_{ax}G_K^{ax} + \Delta\chi_{rh}G_K^{rh}) \tag{2}$$

where $\Delta\chi_{ax}$ and $\Delta\chi_{rh}$ are the axial and rhombic components of the molar magnetic susceptibility tensor $\boldsymbol{\chi}$, N_A the Avogadro constant and G_K^{ax} and G_K^{rh} the axial and rhombic geometric factors. χ_{xx}, χ_{yy} and χ_{zz} are the three principal components of the χ tensor, $\Delta\chi_{ax} = \chi_{zz} - \dfrac{(\chi_{xx}+\chi_{yy})}{2}$ and $\Delta\chi_{rh} = \chi_{xx} - \chi_{yy}$. In this work, we follow the convention where χ_{xx} and χ_{yy} are chosen so that $\Delta\chi_{ax}$ and $\Delta\chi_{rh}$ have opposite signs.[9] The two geometric factors are defined by the position of the NMR active nucleus K (x_K, y_K and z_K) in the frame of the principal axes of the $\boldsymbol{\chi}$ tensor as $G_K^{ax} = \dfrac{3z_K^2}{r_K^5} - \dfrac{1}{r_K^3}$ and $G_K^{rh} = \dfrac{3}{2}\dfrac{x_K^2 - y_K^2}{r_K^5}$, r_K being the metal–nucleus distance.

For an axial system, $\chi_{xx} = \chi_{yy}$ ($\Delta\chi_{rh} = 0$) and Eq.(2) simplifies to

$$\delta_K^{pc} = \frac{10^6}{12\pi N_A}\Delta\chi_{ax}G_K^{ax} \tag{3}$$

It follows that for an axial complex with dominant dipolar contribution, the AIS are proportional to the geometrical factor. As a starting point, due the strong anisotropy of the $[An^{VI}O_2]^{2+}$ and $[Np^{V}O_2]^{+}$complexes, the z axis is placed along the $An^{V/VI}$-O_{yl} bond. The $\boldsymbol{\chi}$

tensor will further be fully determined from *ab initio* calculations and this will confirm this hypothesis.

In this section, we will compare the pNMR shifts calculated for the selection of conformations discussed previously to the experimental values. We will analyze to what extent we can assign these different conformations and also study the transferability of the magnetic anisotropy of the $Np^{V/VI}$ and Pu^{VI} complexes according to the equatorial ligands.

Axial dipolar equation

Experimental ^{1}H chemical shifts of $[An^{VI}O_2(TEDGA)(H_2O)_x]^{2+}$, $[An^{VI}O_2(TEDGA)_2]^{2+}$ and $[Np^{V}O_2(TEDGA)_2]^{+}$ species were collected at 298 K in CD_3CN . The paramagnetic ^{1}H and ^{13}C NMR chemical shifts deduced by using uranium complexes as diamagnetic reference are reported in Table 3. When the paramagnetic shifts only arise from dipolar interactions, in the case of an axial symmetry, the ratio $R_{KK'}$ between two nuclei K and K' as expressed by Eq.(3) simplifies to the ratio of their axial geometric factors

$$R_{KK'} = \frac{\delta^p_K}{\delta^p_{K'}} = \frac{G^{ax}_K}{G^{ax}_{K'}} \tag{4}$$

The ratio of the experimental AIS at 298 K are compared to the ratio of the axial geometric factors for the different $[An^{VI}O_2(TEDGA)_2]^{2+}$, $[An^{VI}O_2(TEDGA)(H_2O)_2]^{2+}$ and $[Np^{V}O_2(TEDGA)_2]^{+}$ selected structures in Table S7. Further on, Eq.(3) allows a first estimation of $\Delta\chi_{ax}$ as given in Table 4. For the 1:2 complexes, the deviations (σ values Table S7) are larger than usually expected for actinyle cations within the dipolar approximation (from 5 to 36% for ^{1}H and about 17% for ^{13}C). Small standard deviations are however obtained for the 1:1 complex. As shown by MD simulation, 1:2 complexes exist in a large number of conformations with two different coordination modes and one can expect a mixture of them in solution while the 1:1 stoichiometry presents a reduced number of conformers.[25] The selected conformations (6c(TTT), 6c(CCC) or 5c(TTT)) are consequently not representative

enough of the mixture in solution and this can explain the quite high standard deviations. Surprisingly, the 5c(T) structure, that does not have an axial symmetry, leads to the lowest standard deviation for the 1:1 complex whatever the cation (Np^{VI}, Pu^{VI}) is. This shows first, that the axial symmetry of the actinyl cation still holds in the case where equatorial ligands break the axial symmetry, and secondly, that the observed AIS result firstly from dipolar interactions and in the case of the 1:2 stoichiometry, they arise from a large number of conformations which can hardly modelized by one of the three selected conformations.

Table 3: Experimental ^{1}H and ^{13}C AIS in ppm of $[An^{VI}O_2(TEDGA)_2]^{2+}$ and $[An^{VI}O_2(TEDGA)(H_2O)_2]^{2+}$ complexes (An = Np and Pu) at 298 K in CD_3CN. Diamagnetic shifts are available in Tables S5 and S6. TMS in CD_3CN is used as reference.

		$\delta^p_{H_1}$	$\delta^p_{H_2}$	$\delta^p_{H_3}$	$\delta^p_{H_4}$	$\delta^p_{H_5}$
$[An^{VI}O_2(TEDGA)_2]^{2+}$	Np^{VI}	-17.616	-11.271	-5.567	-7.198	-4.133
	Pu^{VI}	-46.498	-34.888	-17.01	-20.31	-11.545
$[An^{VI}O_2(TEDGA)(H_2O)_x]^{2+}$	Np^{VI}	-17.762	-11.191	-6.313	-7.139	-4.104
	Pu^{VI}	-52.245	-36.188	-19.432	-22.286	-12.341
$[Np^{V}O_2(TEDGA)_2]^{+}$		-47.754	-36.636	-20.115	-20.548	-11.518

	$\delta^p_{C_1}$	$\delta^p_{C_2}$	$\delta^p_{C_3}$	$\delta^p_{C_4}$	$\delta^p_{C_5}$	$\delta^p_{C_6}$
$[Np^{VI}O_2(TEDGA)_2]^{2+}$	-32.731	-13.576	-7.386	-5.997	-4.268	-41.76

Regarding the $[Np^{V}O_2(TEDGA)_2]^{+}$ complex the larger deviation (19%) observed for the 6c conformations could be due to the use of the twice charged species $[U^{VI}O_2(TEDGA)_2]^{2+}$ as diamagnetic reference instead of the $Pa^{V}O_2(TEDGA)_2]^{+}$ compound which is not available at lab.

From these $R_{KK'}$ analysis and as expected from our previous study dealing with the DPA ligand[19], it comes out that AIS arising from ^{1}H or ^{13}C do not contain significant contact contribution and are then dipolar in origin. In the next section we will investigate further about this axial symmetry simplification by including the rhombic contribution to the description of the pseudocontact shifts.

Effect of the non-axial symmetry

As some deviations are observed in using Eq.(3), it is interesting to explicitly take into account the rhombic contribution with Eq.(2) in order to check a breakdown in the axiality assumption. We therefore determined the rhombic contribution to the $\boldsymbol{\chi}$ tensor. On one hand, it is achieved by diagonalizing the $\boldsymbol{\chi}$ tensor calculated by *ab initio* methods, as given in Table S24. On the other hand, it is deduced by fitting the AIS with Eq.(2). To apply this equation, one should know the principal axes of the $\boldsymbol{\chi}$ tensor. The 6c $[Np^{VI}O_2(TEDGA)_2]^{2+}$ conformers denote a symmetry close to $\mathcal{D}_{2h}$ and those axes are considered to be the principal ones, even for the 5c conformer. This hypothesis is further verified by the *ab initio* calculations. The results are compared in Tables 4 and 5 for the $5f^1$ and $5f^2$ complexes respectively.

Table 4: Magnetic susceptibility tensor at 298 K (in 10^{-8} $m^3.mol^{-1}$) for the $5f^1$ complexes, deduced from the fit of the AIS and from *ab initio* methods. The fit is performed either using Eq.(3) (ax) or Eq.(2) (ax-rh), and using either ^{1}H AIS or both ^{1}H and ^{13}C AIS. Q_{pc} characterizes the standard deviation of the fitting procedure (see Eq.(S5)). Calculated ^{1}H and ^{13}C pNMR shifts are available in Table S8.

conformer	method	$\Delta\chi_{ax}$	$\Delta\chi_{rh}$	Q_{pc}
	$[Np^{VI}O_2(TEDGA)_2]^{2+}$			
6c(TTT)	ax ^{1}H	3.8	-	7%
	ax ^{13}C	3.8	-	5%
	ax-rh ^{1}H + ^{13}C	3.8	-0.1	5%
	SO-CASPT2	4.0	-0.15	
	SO-RASPT2	4.9	-0.16	
6c(CCC)	ax ^{1}H	4.3	-	16%
	ax ^{13}C	4.2	-	8%
	ax-rh ^{1}H + ^{13}C	4.0	-0.4	6%
	SO-CASPT2	4.0	-0.14	
	SO-RASPT2	5.0	-0.15	
5c(TTT)	ax ^{1}H	4.0		20%
	ax ^{13}C	4.3	-	12%
	ax-rh ^{1}H + ^{13}C	3.8	-0.6	7%
	SO-CASPT2	1.6	-0.04	
	SO-RASPT2	2.8	-0.06	
	$[Np^{VI}O_2(TEDGA)(H_2O)_2]^{2+}$			
5c(T)	ax ^{1}H	3.7	-	3%
	ax-rh ^{1}H	3.7	-0.06	2%
	SO-CASPT2	4.6	-0.11	
	SO-RASPT2	5.6	-0.09	

Considering the rhombic contribution strongly improves the fit despite $\Delta\chi_{rh}$ values are at least one order of magnitude lower than $\Delta\chi_{ax}$. The axial contribution is slightly affected, while the rhombic component is the largest in cases where the standard deviation for the only axial component is the largest. The rhombic component is supposed to describe the

non-axiality but can also be used to compensate a conformation that does not suit the experimental AIS. Indeed, in order to determine the susceptibility tensor $\boldsymbol{\chi}$ for a given conformer, we should have the AIS of the pure conformer while we have only the AIS for a mixture of conformers. The values for $\Delta\chi_{ax}$ are rather similar for all $5f^1$ complexes, around 4 ± 0.2 10^{-8} $m^3.mol^{-1}$. It is because all the fits are performed with the same AIS, and we can conclude that if one conformer is dominating, its $\Delta\chi_{ax}$ is close to this value. According to *ab initio* calculations, the 6c(TTT) and 6c(CCC) have very similar $\boldsymbol{\chi}$ tensors. Indeed, those two conformers have similar coordination spheres. This follows the similar compositions of the ground KD for the two conformers (see Table S22). The tensor is strongly axial with the easy axis along the yle bond. In the equatorial plane, the y axis pointing towards the O2 atom of the TEDGA ligand is slightly less magnetic than the direction pointing in between the two TEDGA leading to a small rhombic $\Delta\chi_{rh}$ of about -0.15 10^{-8} $m^3.mol^{-1}$. The *ab initio* $\Delta\chi_{ax}$ for the 5c(TTT) conformer is smaller than for the two previous conformers. The $\boldsymbol{g}$ tensor of the ground KD is indeed little anisotropic, with almost the same three g factors. It can be seen from Table S25 that the main contribution to the $\boldsymbol{\chi}$ tensor arises from the coupling between the two lowest KDs (parameter ΔM_{12}), the so-called Van Vleck contribution. The rhombic contribution is smaller than for the 6c conformers and the axis with the smallest value points towards the O2 atom, with a small angle (20°). This 5c(TTT) is certainly not representative of the conformation mainly observed at NMR time scale and explains the large $\Delta\chi_{rh}$ deduced from AIS.

Table S19 presents the magnetic susceptibility components determined with all the MD conformations of each conformers using Eq.(2) and the associated deviation. We can see that all conformers have a similar component for the same cation, contrary to what was determined with the DFT optimized conformations (Tables 4 and 5), showing the importance of taking into account all conformations of each conformer. In addition, the $\Delta\chi_{ax}$ values are closer to the CASPT2 values, with less than 10% of difference.

Table 5: Magnetic susceptibility tensor at 298 K (in 10^{-8} $m^3.mol^{-1}$) for the $5f^2$ complexes, deduced from the fit of the ^{1}H AIS and from SO-CASPT2. The fit is performed either using Eq.(3) (ax) or Eq.(2) (ax-rh). Q_{pc} chararterizes the standard deviation of the fitting procedure (see Eq.(S5)). Calculated ^{1}H pNMR shifts are available in Table S9.

conformer	method	$\Delta\chi_{ax}$	$\Delta\chi_{rh}$	Q_{pc}
$[Pu^{VI}O_2(TEDGA)_2]^{2+}$				
6c(TTT)	ax ^{1}H	10.8	-	4%
	ax-rh ^{1}H	10.8	-0.004	4%
	SO-CASPT2	13.3	0	
6c(CCC)	ax ^{1}H	12.2	-	10%
	ax-rh ^{1}H	12.1	-0.76	4%
	SO-CASPT2	13.3	0	
5c(TTT)	ax ^{1}H	11.2	-	16%
	ax-rh ^{1}H	11.1	-0.99	11%
	SO-CASPT2	13.6	0	
$[Pu^{VI}O_2(TEDGA)(H_2O)_2]^{2+}$				
5c(T)	ax ^{1}H	11.2	-	3%
	ax-rh ^{1}H	11.3	-0.16	2%
	SO-CASPT2	13.5	0	
$[Np^{V}O_2(TEDGA)_2]^{+}$				
6c(TTT)	ax ^{1}H	12.2	-	7%
	ax-rh ^{1}H	12.2	-0.004	7%
	SO-CASPT2	13.9	0	
5c(TTT)	ax ^{1}H	11.5	-	15%
	ax-rh ^{1}H	11.5	-0.1	10%
	SO-CASPT2	14.1	0	

Finally, the 1:1 complex denotes a $\boldsymbol{\chi}$ tensor close to the 1:2 6c(TTT) Np^{VI} complexes with a slightly larger value for *ab initio* $\Delta\chi_{ax}$. It clearly comes out that the $\Delta\chi_{rh}$ component is not mainly related to the non-axiality of the complex since the 1:1 and 5c 1:2 have a smaller rhombic contribution than the 6c 1:2 conformers which are more axial.

The axial component $\Delta\chi_{ax}$ of the $5f^2$ cations appears to be roughly independent on the equatorial ligand unlike the $5f^1$ ones. Due to this weak sensitivity, experimental $\Delta\chi_{rh}$ values of the $5f^2$ cations are more sensitive to experimental inaccuracies (variations of $\Delta\chi_{rh}$ from -0.004 to -0.99 10^{-8} $m^3.mol^{-1}$ depending on the selected conformer for one set of AIS, see Table 5). The sensitivity of the $5f^1$ electronic configuration is confirmed by *ab initio* calculations. Indeed, with the $[Np^{VI}O_2(TEDGA)_2]^{2+}$ complex, $\Delta\chi_{ax}$ *ab initio* values depend on the method and the conformation used (from 2.1 to 5.6 10^{-8} $m^3.mol^{-1}$ see Table S24). This contrasts with the $5f^2$ cations where similar $\Delta\chi_{ax}$ values are obtained (13.8 ± 0.4 10^{-8} $m^3.mol^{-1}$) whatever the methods (SO-CASSCF or SO-CASPT2) despite they are about 15% overestimated compared to the experimental values.

Temperature dependence of the pNMR shifts

Dependence of ^{1}H pNMR shifts with temperature is recorded in the $220-350$ K range and shown in Figure 4 for $[Np^{VI}O_2(TEDGA)_2]^{2+}$ and $[Pu^{VI}O_2(TEDGA)_2]^{2+}$ complexes. ^{13}C pNMR are also collected but only for the Np^{VI} complex because Pu^{VI} complexes ^{13}C signals are too broad and/or weak to be observed. $\Delta\chi_{ax}$ and $\Delta\chi_{rh}$ are deduced from Eq.(2) for each temperature using the 6c(TTT) conformation since it is the more likely one (the more stable conformation from DFT calculations (see Table 2) and with the lowest Q_{pc} values) for both Np and Pu complexes. The resulting $\Delta\chi_{ax}$ and $\Delta\chi_{rh}$ are plotted as a function of 1/T in Figure 5. Both axial and rhombic anisotropic terms follow a 1/T law (correlation coefficient r>0.998).

In our previous work on $[Np^{VI}(DPA)_3]^{2+}$, the fitting of the temperature dependence of the $\Delta\chi_{ax}$ component using Eq.(S7) allowed to characterize the two lowest KDs; we determined the magnetic anisotropy of the two lowest KDs, Δg_1^2 for KD1, Δg_2^2 and for KD2 ($\Delta g_I^2 = g_{I\parallel}^2 - g_{I\perp}^2$), the axial Van Vleck term $\Delta M_{12}^2 = M_{12\parallel}^2 - M_{12\perp}^2$ and the energy separation between the two KDs Δ.[19] However, the linear dependence of $\Delta\chi_{ax}T$ against T suggests that the second KD is not populated at room temperature which is confirmed by the value of the

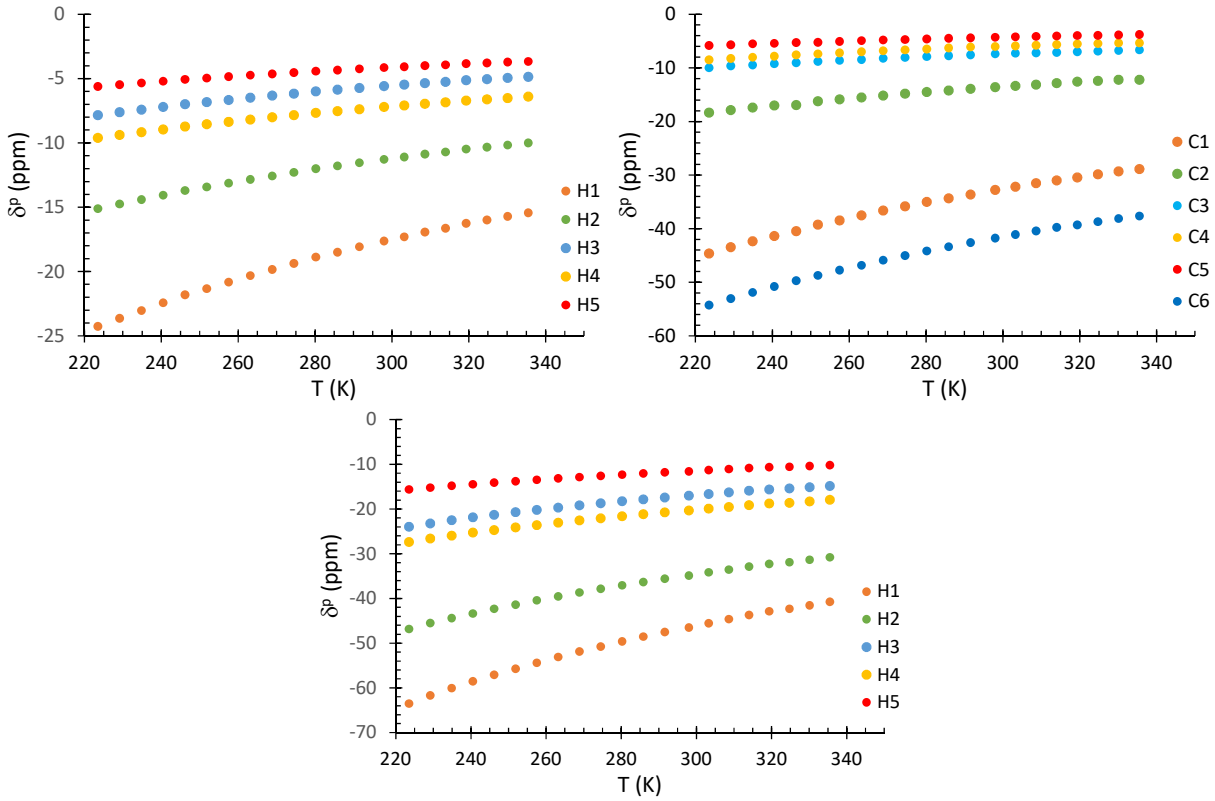

Figure 4: ^{1}H and ^{13}C pNMR shifts of the $[Np^{VI}O_2(TEDGA)_2]^{2+}$ complex (top) and ^{1}H pNMR shifts of the $[Pu^{VI}O_2(TEDGA)_2]^{2+}$ complex (bottom) with temperature in CD_3CN.

energy gap Δ determined from SO-RASPT2 of 600 cm^{-1}. In this limit, KD2 contributes to temperature independent paramagnetism (TIP) and Eq.(S7) reduces to:

$$\Delta\chi_{ax} = N_A\mu_0\mu_B^2\left[\frac{\Delta g_1^2}{4kT} + \frac{\Delta M_{12}^2}{\Delta}\right] \tag{5}$$

where μ_B is the Bohr magneton, μ_0 the magnetic permeability and k the Boltzmann constant. The same equation is obtained for the rhombic contribution replacing Δg_1^2 by $\Delta g_{rh1}^2 = g_x^2 - g_y^2$ and M_{12}^2 by $M_{rh12}^2 = M_x^2 - M_y^2$. Fitting the $\Delta\chi_{ax}$ and $\Delta\chi_{rh}$ of Figure 5 according to Eq.(5) provides the axial Δg_1^2 and rhombic Δg_{1rh}^2 magnetic anisotropies of the ground KD and the $\frac{\Delta M_{12}^2}{\Delta}$ ratio given in Table 6. Fitting of the $\Delta\chi_{ax}$ with the two-KDs model equation (S7) does not provide stable Δg_2^2, ΔM_{12}^2 and Δ parameters, but the parameter associated to KD1 Δg_{1ax}^2 is stable and close to the one-KD model parameter which further highlights that

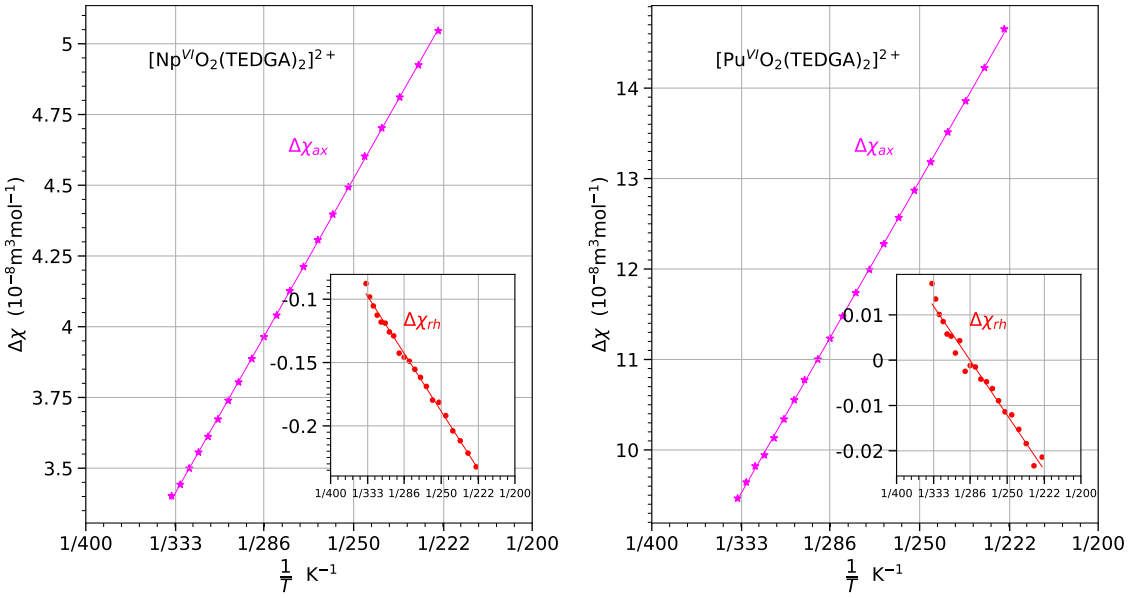

Figure 5: Magnetic susceptibility anisotropy ($\Delta\chi_{ax}$ (main), $\Delta\chi_{rh}$ (inset)) of the $[Np^{VI}O_2(TEDGA)_2]^{2+}$ (left) and $[Pu^{VI}O_2(TEDGA)_2]^{2+}$ (right) complexes in 10^{-8} $m^3.mol^{-1}$. Values are obtained from ^1H and ^{13}C AIS with temperature for the former and only ^1H pNMR shifts for the later considering the 6c(TTT) geometry.

KD2 is not populated. This explains the observed 1/T dependence of the $\Delta\chi_{ax}$ and $\Delta\chi_{rh}$. The fitted model parameters are in quite good agreement with the *ab initio* results since axial and rhombic Δg_1^2 and $\Delta M_{12}^2/\Delta$ values are all in the same magnitude order. The main contribution given by Δg_1^2 only differs from 20% with the experimental fitting (See Figure S15 for comparison).

In the case of the $5f^2$ $[Pu^{VI}O_2(TEDGA)_2]^{2+}$ complex, the anisotropic magnetic susceptibility is modeled with the energetically well isolated ground NKD and the excited state contributions are very small. For a NKD, the two states are not necessarily degenerate, one only considers the Van Vleck contribution in Eq.(S8) where the magnetic interaction of a NKD is modeled with the unique non-zero g-factor $g_\parallel$. *Ab initio* calculations suggest that the splitting of the NKD is very small and the axial anisotropy of the magnetic susceptibility can be modeled as

$$\Delta\chi_{ax} = N_A\mu_0\mu_B^2\frac{g_\parallel^2}{4kT} + TIP \tag{6}$$

Table 6: Model parameters evaluated from *ab initio* calculations for the $[An^{VI}O_2(TEDGA)_2]^{2+}$ complexes and compared to those deduced by fitting the temperature dependent $\Delta\chi$ curves (Figure 5). $\Delta M_{12}^2/\Delta$ is in μ_B^2/cm^{-1}.

$[Np^{VI}O_2(TEDGA)_2]^{2+}$ 6c(TTT)				
Method	Δg_1^2	Δg_{rh1}^2	$\Delta M_{12}^2/\Delta$	$\Delta M_{rh12}^2/\Delta$
fit $\Delta\chi_{ax}$	9.45	-	0.006	-
fit $\Delta\chi_{rh}$	-	-0.77	-	0.017
SO-RASPT2	11.83	-0.46	0.001	0.00
$[Pu^{VI}O_2(TEDGA)_2]^{2+}$ 6c(TTT)				
fit $\Delta\chi_{ax}$	29.4	-	-	-
SO-CASPT2	35.46	-	-	-

Fitting of the experimental $\Delta\chi_{ax}$ obtained from the temperature dependent ^{1}H pNMR shifts in the $[Pu^{VI}O_2(TEDGA)_2]^{2+}$ complex provides $g_{\|}$ (and the corresponding Δg^2) associated to the magnetic moment of the NKD (Table 6). A good agreement is observed with the *ab initio* values despite Δg_1^2 is about 20% greater than the fitted one. This overestimation is also observed for Np^{VI}. From a theoretical point of view the null TIP value expected in the Pu^{VI} complex case is confirmed experimentally. Fitted and *ab initio* $\Delta\chi_{ax}$ and $\Delta\chi_{rh}$ are compared Figure S15.

Comparison between the TEDGA and DPA ligands

In this work, we determined the values of $\Delta\chi_{ax}$ from AIS for the TEDGA derivatives, and it is of interest to compare them to the DPA derivatives.[19] With the $[Np^{VI}O_2]^{2+}$ cation, $\Delta\chi_{ax}$ is found to be 4.0±0.2 and 2.2±0.1 for the TEDGA and DPA ligands respectively (values are given in $10^{-8}m^3.mol^{-1}$ and deduced as an average on the conformations for the TEDGA derivatives). With the $[Pu^{VI}O_2]^{2+}$, we found 11.9±0.5 and 10.1±0.2 for the TEDGA and DPA ligands respectively and finally, 11.4±0.7 for the $[Np^{V}O_2(TEDGA)_2]^{+}$ complex. $\Delta\chi_{ax}$ denotes larger variations for the $5f^1$ $[Np^{VI}O_2]^{2+}$ cation than for the $5f^2$

$[Np^{V}O_2]^+$ and $[Pu^{VI}O_2]^{2+}$ ones (45% and 15% respectively). As developped in Section S4.2 in the SI, the $5f^2$ electronic configuration is less sensitive to the equatorial ligand, with one electron in the $5f_\delta$, and one in the $5f_\phi$ orbital, in order to minimize the electron-electron interaction. This leads to a ground state close to the $^3H_4$ term of the free actinyl cation, whatever the ligands in the equatorial plane are.

On the contrary, for the $5f^1$ configuration, the nature of the ground state is determined by the subtle mixing in terms of $5f_\delta$ and $5f_\phi$ orbitals. This mixing is sensitive to the level of calculation. At SO-RASPT2 level, the $5f_\phi/5f_\delta$ ratio is 70/30 (Table S22) with the TEDGA ligand while it is 37/62 (Table 5)[19] with DPA^{2-} despite the ternary symmetry of the two complexes. Even if in the two cases the susceptibility tensor is eventually prolate, the mechanisms are different: with the TEDGA ligand, only one KD participates with a prolate magnetization (Δg_1^2 positive) while with the DPA^{2-} ligand, the ground KD has an oblate magnetization (Δg_1^2 negative), but the interaction with the second KD is dominant and prolate (Van Vleck contribution).

Conclusion

In this work ^1H and ^{13}C paramagnetic chemical shifts of Actinyl-TEDGA systems are measured and analyzed with the help of *ab initio* calculations, XRD results, MD simulations[25] and compared to published $[An^{VI}O_2]^{2+}$-DPA complexes.[19] We considered the $5f^1$ and $5f^2$ electronic configurations of the actinyl cation complexed with two TEDGA ligands, $[An^{V/VI}O_2(TEDGA)_2]^{+/2+}$. The case where one TEDGA ligand is replaced by water molecules, $[An^{VI}O_2(TEDGA)(H_2O)_x]^{2+}$, was considered in order to lower the symmetry. As highlighted by a previous study based on MD simulations, the TEDGA ligand is flexible and the complexes exist in both six- and five coordinated modes. In order to perform CAS based calculations, a set of conformations has been selected based on the MD simulations and optimized using DFT. Since the TEDGA ligand is a flexible ligand, it is difficult to perform an

ab initio study of the magnetic susceptibility tensor considering all conformations reflecting observed AIS. Previous MD simulations were helpful in the selection of conformations.[25] A set of representative conformations has been selected in order to probe geometrical effects. The *ab initio* calculations show that the six-coordinated species is the lowest in energy and that all conformations have an axial $\boldsymbol{\chi}$ tensor with a negligible rhombicity, even for those where the symmetry of the coordination sphere has been lowered. It shows that the strong axiality of the yle bond keeps prevailing. The $\Delta\chi_{ax}$ value depends on the conformation on the equatorial ligands for the $5f^1$ complexes but is rather insensitive in the case of $5f^2$ complexes. This feature, suggests that a structural study of $5f^2$ actinyl complexes (Pu^{VI} and Np^{V}) can be performed considering first, a dominant dipolar contribution in the AIS, secondly a negligible rhombic term and thirdly a $\Delta\chi_{ax}$ value of about 11.6 10^{-8}m^3.mol^{-1} (in 10% accuracy) as a good approximation. Such a feature can not be set for $5f^1$ actinyl (Np^{VI} complexes) despite a pure dipolar contribution can be reasonably applied for ^{1}H and ^{13}C AIS analysis. For flexible ligands, observed AIS result from numerous conformations and it is of main importance to take them into account or at least the most representative ones. The MD which is an efficient tool for this purpose, requires χ components ($\Delta\chi_{ax}$, $\Delta\chi_{rh}$) to be insensitive to conformation changes during the simulation. This property is fully satisfied for the $5f^2$ actinyl but is not necessary valid for the $5f^1$ actinyl (Np^{VI}).

Experimental and computational section

Synthesis

Caution!!! ^{238}Uranium, ^{237}Neptunium and $^{239+240}$Plutonium are radioactive elements and have to be handled in dedicated facilities with appropriate equipment for radioactive materials. Their manipulation has been carried out at the ATALANTE facility (CEA-Marcoule, France). The experiments involving Np and Pu were performed in a regular air atmosphere negative pressure glove box with restrictive protocols, whereas U was manipulated

under fume hood. Tetramethylammonium and Tetraethylammonium chloride ($(CH_3)_4NCl$, $(C_2H_5)_4NCl$ noted TMACl and TEACl respectively), silver +II oxide ($Ag^{II}O$), silver trifluoromethanesulfonate ($AgCF_3SO_3$, noted AgOTf), HCl 37%, tetrahydrofuran (THF) and acetonitrile (CH_3CN) were purchased from Sigma-Aldrich and used as received. For NMR needs, CD_3CN was used (Sigma-Aldrich ref. 366544): 99.8 atom % D and containing 0.03% v/v of TMS. TEDGA was provided by Pharmasynthese (Lisses, France).

$[R_4N]_2An^{VI}O_2Cl_4$ reagent synthesis (R=CH_3, C_2H_5):

$(C_2H_5)_4NCl$ has been mainly used as reagent but $(CH_3)_4NCl$ has also advantageously been used to avoid some ^1H signal overlap with the tBuOH (terbutanol) peak for magnetic susceptibility measurements. Both ammonia cations lead to the same actinide complexes only their solubility change slightly in acetonitrile. A solution of U^{VI} was prepared by dissolving solid $U^{VI}O_3$ in 3mol.L^{-1}HCl; a solution of Np^V was prepared by dissolving solid Np^VO_2OH in 1mol.$L^{-1}HNO_3$; the initial plutonium solution was Pu^{IV} in 1mol.$L^{-1}HNO_3$. Np^V and Pu^{IV} were oxidized by adding $Ag^{II}O$ (molar ratio Np^V:$Ag^{II}O$ of 1:5 and molar ratio Pu^{IV}:$Ag^{II}O$ of 1:10) to prepare Np^{VI} and Pu^{VI} nitrate solutions. Oxidation states and concentrations of actinide solutions were checked by visible-NIR spectrophotometry (Agilent Cary 5000 spectrophotometer). AgCl was precipitated subsequently by adding a stoichiometric amount (relative to Ag^{II} reagent) of HCl and the resulting white solid was removed by centrifuge. The resulting solutions were successively evaporated three times with addition of HCl 37% to remove residual nitric acid. The solid compounds obtained from the last evaporation were dissolved in 3mol.L^{-1}HCl. To these solutions were added two equivalents of $(C_2H_5)_4NCl$ and left to evaporation under N_2 [27]. The deposition of $[(C_2H_5)_4N]_2An^{VI}O_2Cl_4$ were washed twice with THF and dried at room temperature under N_2 flow. The same protocol was applied for the $[(CH_3)_4N]_2An^{VI}O_2Cl_4$ synthesis.

NMR spectroscopy

^{1}H NMR spectra were recorded using 400 MHz Fourier transform spectrometer, Agilent DD2, set up for the study of radioactive samples[28]. Acquisitions and processing were performed with OpenVnmrJ 2.1 software[29]. A 5mm probe 'OneProbe' with Z-gradient has been used. The spectra of $[An^{VI}O_2]^{2+}$-TEDGA complexes were collected at 252 K and room temperature to ensure slow exchange occurs between free and complexed ligands.

SC-XRD

Each crystal was mounted on MicroMount patented by MiTeGen, inserted into a goniometer base. To prevent actinide health hazards, a MicroRT capillary was then drawn over the sample and onto the base, where it was sealed by adhesive. The single-crystal XRD intensities were measured on a Bruker D8 Quest diffractometer equipped with a Photon II detector coupled device at 100 K using a 800 series cryostreamcooler (Oxford Cryosystem). The instrument was equipped with a Mo-target ImS Mircofocus source (l=0.71073Å). Data were collected using phi and omega scans, with 0.7° frame widths. Intensities were extracted from the collected frames using the program SaintPlus[30]. The unit cell parameters were refined from the complete data set, and a multi-scan absorption correction was performed[31]. The structure determination and refinement were realized with ShelX-2017 softwares[32]. The heavy atoms were located by direct methods while the remaining atoms were found from successive Fourier map analyses. All of the nonhydrogen atoms were located and their positions were refined anisotropically. Hydrogen atoms were placed in calculated positions refined using idealized geometries (riding model) and assigned fixed isotropic displacement parameters. $An^{VI}O_2(TEDGA)_2(CF_3SO_3)_2$ with An=U, Np and Pu and $Np^{V}O_2(TEDGA)_2(NO_3)$ cif files are provided in SI.

Computational details

The geometry calculations were performed with Gaussian09[33] within the density functional theory (DFT) framework using the hybrid B3LYP functional[34]. For Uranium, Stuttgart relativistic large-core (RLC) basis set with the corresponding pseudo-potential[35] and 6-31G(d-p)[36] basis sets for the light atoms were used. Acetonitrile solvent effects were included implicitly with a polarizable continuum model and Grimme's dispersion energy correction was introduced with D3 approach[37]. All the optimized geometries were checked to be true minima by a frequency calculation. The difference in energy between two structures includes zero-point energy correction. Structure visualization and coordinates handling were performed with Chemcraft software[38].

All wavefunction based calculations have been performed on the crystallographic structures for $[An^{VI}(TEDGA)_2]^{2+}$ complexes and optimized structures for $[An^{VI}(TEDGA)(H_2O)_2]^{2+}$ complexes with the MOLCAS 7.8 suite of software.[39] First, CASSCF (Complete Active Space Self Consistent Field)[40] calculations were performed with an active space consists of six valence $5f$ orbitals and n associated electrons *i.e.* CAS (n,6). An extended active space was considered for the neptunyl complexes using the RASSCF (Restricted Active Space Self Consistent Field) scheme; the bonding and anti-bonding σ and π orbitals of the yl bonds were included in RAS1 and RAS3 spaces, respectively, considering all the possible configurations generated by $2h-2p$ excitation.[41] The amount of electron dynamic correlation included has a greater influence on the electronic structure and magnetic properties of the $5f^1$ actinyl complexes, which is why the RASSCF technique is only explored for the neptunyl complexes.[19] Perturbative treatment of the dynamic correlation was considered with the CASPT2 (Complete Active Space Perturbation Theory at 2nd order)[42] method using the CASSCF or RASSCF wavefunctions as the reference states[43] without any level shift. Relativistically contracted ANO (Atomic natural Orbitals)[44,45] basis sets were used for the calculations with TZP quality for Np, Pu, O ; DZP for C and DZ for H atoms. Douglas-Kroll-Hess (DKH2) transformed Hamiltonian[46,47] was used to treat the relativistic effects

for both scalar (SR) and spin-orbit (SO). 6 doublets were considered for the Np^{VI} complex and 15 triplets and 21 singlets for the Pu^{VI} complexes. Spin-orbit coupling (SOC) was calculated as a state interaction between either with CASSCF or RASSCF wavefunctions and corresponding energies leading to the so-called SO-CASSCF and SO-RASSCF results or with MS-CASPT2 or MS-RASPT2 wavefunctions and corresponding energies, leading to the so-called SO-CASPT2 and SO-RASPT2 results. Two-electron SO integrals were computed using one-center approximations with AMFI (Atomic Mean Field Integrals)[48] approach. g factors were calculated according to ref.[49] and the molar magnetic susceptibility tensor $\boldsymbol{\chi}$ according to ref.[50]. The semi-core $5p$ and $5d$ orbitals needed to be correlated during perturbation calculation as highlighted in our previous publication on $[Np^{VI}O_2(DPA)_2]^{2-}$ complex.[19]

Acknowledgement

This work was in part supported by the French ANR under convention N° ANR-17-CE06-0010.

Supporting Information Available

The Supporting Information contains geometric structure of the complexes with CCDC accession codes, MD simulations data, DFT optimized structures, analysis of the conformers, NMR spectroscopy data, magnetic susceptibility tensor deduced from AIS, from MD analysis and modelization from temperature dependence. Energy levels, magnetic susceptibility tensor are provided from different *ab initio* calculation methods.

References

(1) Bleaney, B. Nuclear magnetic resonance shifts in solution due to lanthanide ions. *J. Magn. Reson.* **1972**, *8*, 91–100.

(2) Reilley, C. N.; Good, B. W.; Allendoerfer, R. D. Separation of Contact and Dipolar Lanthanide Induced Nuclear Magnetic Resonance Shifts: Evaluation and Application of Some Structure Independent Methods. *Anal. Chem.* **1976**, *48*, 1446–1458.

(3) Desreux, J. F.; Reilley, C. N. Evaluation of Contact and Dipolar Contributions to ^{1}H and ^{13}C Paramagnetic NMR Shifts in Axially Symmetric Lanthanide Chelates. *J. Am. Chem. Soc.* **1976**, *98*, 2105–2109.

(4) McGarvey, B. R. Temperature dependence of the pseudocontact shift in lanthanide shift reagents. *Journal of Magnetic Resonance (1969)* **1979**, *33*, 445–455.

(5) Reuben, J. Structural information from chemical shifts in lanthanide complexes. *Journal of Magnetic Resonance (1969)* **1982**, *50*, 233–236.

(6) Sherry, A.; Singh, M.; Geraldes, C. Nuclear magnetic resonance structural studies of an axially symmetric lanthanide ion chelate in aqueous solution. *Journal of Magnetic Resonance (1969)* **1986**, *66*, 511–524.

(7) Bertini, I.; Luchinat, C. Why another book on NMR? *Coord. Chem. Rev.* **1996**, *150*, ix.

(8) Clore, M., Potts, J., Eds. *Recent developments in biomolecular NMR*; RSC Biomolecular Sciences; The Royal Society of Chemistry, 2012.

(9) Bertini, I.; Luchinat, C.; Parigi, G.; Ravera, E. *NMR of Paramagnetic Molecules. Applications to Metallobiomolecules and Models*, 2nd ed.; Current Methods in Inorganic Chemistry; Elsevier Science, 2016; Vol. 2.

(10) Ravera, E.; Parigi, G.; Luchinat, C. What are the methodological and theoretical prospects for paramagnetic NMR in structural biology? A glimpse into the crystal ball. *J. Magn. Reson.* **2019**, *306*, 173–179.

(11) Pemmaraju, C. D.; Copping, R.; Smiles, D. E.; Shuh, D. K.; Grønbech-Jensen, N.; Prendergast, D.; Canning, A. Coordination Characteristics of Uranyl BBP Complexes: Insights from an Electronic Structure Analysis. *ACS Omega* **2017**, *2*, 1055–1062.

(12) Li, P.; Wei, H.; Duan, M.; Wu, J.; Li, Y.; Liu, W.; Fu, Y.; Xie, F.; Wu, Y.; Ma, J. Actinyl-Carboxylate Complexes $[AnO_2(COOH)_n(H_2O)_m]_n^{2-}$ (An = U, Np, Pu, and Am; n = 1–3; m = 0, 2, 4; 2n + m = 6): Electronic Structures, Interaction Features, and the Potential to Adsorbents toward Cs Ion. *ACS Omega* **2020**, *5*, 31974–31983.

(13) Choppin, G.; Liljenzin, J.-O.; Rydberg, J.; Ekberg, C. In *Radiochemistry and Nuclear Chemistry*, 4th ed.; Elsevier,, Ed.; Academic Press, 2013.

(14) Begg, J. D.; Zavarin, M.; Kersting, A. B. Desorption of plutonium from montmorillonite: An experimental and modeling study. *Geochimica et Cosmochimica Acta* **2017**, *197*, 278–293.

(15) Romanchuk, A. Y.; Vlasova, I. E.; Kalmykov, S. N. Speciation of Uranium and Plutonium From Nuclear Legacy Sites to the Environment: A Mini Review. *Frontiers in Chemistry* **2020**, *8*, 630.

(16) Zhang, P.; Wang, Y.-X.; Zhang, P.; Wang, S.-A.; Hu, S.-X. Evaluation of Chemical Bonding in Actinyl(VI/V) Oxo-Crown-Ether Complexes for Actinide Series from Uranium to Curium. *Inorg. Chem.* **2020**, *59*, 11953–11961, PMID: 32806007.

(17) Autillo, M.; Guerin, L.; Dumas, T.; Grigoriev, M. S.; Fedoseev, A. M.; Cammelli, S.; Solari, P. L.; Guillaumont, D.; Guilbaud, P.; Moisy, P.; Bolvin, H.; Berthon, C. Insight of the Metal–Ligand Interaction in f-Element Complexes by Paramagnetic NMR Spectroscopy. *Chemistry – A European Journal* **2019**, *25*, 4435–4451.

(18) Gendron, F.; Pritchard, B.; Bolvin, H.; Autschbach, J. Magnetic Resonance Properties of Actinyl Carbonate Complexes and Plutonyl(VI)-tris-nitrate. *Inorg. Chem.* **2014**, *53*, 8577–8592.

(19) Autillo, M.; Islam, M. A.; Héron, J.; Guérin, L.; Acher, E.; Tamain, C.; Illy, M.-C.; Moisy, P.; Colineau, E.; Griveau, J.-C.; Berthon, C.; Bolvin, H. Temperature Dependence of ^{1}H Paramagnetic Chemical Shifts in Actinide Complexes, Beyond Bleaney's Theory: The $An^{VI}O_2^{2+}$-Dipicolinic Acid Complexes (An=Np, Pu) as an Example. *Chemistry – A European Journal* **2021**, *24*, 7138–7153.

(20) Leung, A. F.; Wong, E. Y. Electron Paramagnetic Resonance of NpO_2^{2+} in $Cs_2UO_2Cl_4$ and $CsUO_2(NO_3)_3$. *Phys. Rev.* **1969**, *180*, 380–385.

(21) Denning, R.; Norris, J.; Brown, D. The electronic structure of actinyl ions. *Molecular Physics* **1982**, *46*, 287–323.

(22) Gendron, F.; Páez-Hernández, D.; Notter, F.-P.; Pritchard, B.; Bolvin, H.; Autschbach, J. Magnetic Properties and Electronic Structure of Neptunyl(VI) Complexes: Wavefunctions, Orbitals, and Crystal-Field Models. *Chem. Eur. J.* **2014**, *20*, 7994–8011.

(23) Gendron, F.; Sharkas, K.; Autschbach, J. Calculating NMR Chemical Shifts for Paramagnetic Metal Complexes from First-Principles. *J. Phys. Chem. Lett.* **2015**, *6*, 2183–2188.

(24) Gendron, F.; Autschbach, J. Ligand NMR Chemical Shift Calculations for Paramagnetic Metal Complexes: $5f^1$ vs $5f^2$ Actinides. *Journal of Chemical Theory and Computation* **2016**, *12*, 5309–5321, PMID: 27709950.

(25) Poulin-Ponnelle, C.; Duvail, M.; Dumas, T.; Berthon, C. Contribution of Molecular Dynamics in pNMR for the structural determination of An^{V} and An^{VI} complexes in solution. *Inorg. Chem.* **2022**, *61*, 15895—15909.

(26) Bertini, I.; Luchinat, C.; Parigi, G. Magnetic susceptibility in paramagnetic NMR. *Prog. Nucl. Magn. Reson. Spectrosc.* **2002**, *40*, 249–273.

(27) Schnaars, D. D.; Wilson, R. E. Structural and vibrational properties of U(VI)$O_2Cl_4^{2-}$ and Pu(VI)$O_2Cl_4^{2-}$ complexes. *Inorg. Chem.* **2013**, *52*, 14138–14147, PMID: 24256199.

(28) Farnan, I.; Berthon, C. In *SPR-Nuclear Magnetic Resonance*, 1st ed.; Ramesh, V., Ed.; Specialist Periodical Reports (Book 45); Royal Society of Chemistry; Gld edition (May 11, 2016), 2016; Vol. 45; Chapter 3.

(29) OpenVnmrJ, Version 2.1 A). 2020; `https://https://openvnmrj.org/`, Open source software for NMR spectroscopy.

(30) SaintPlus, version 6.22, Madison, WI. 2001; BRUKER Analytical X-ray Systems.

(31) SADABS, version 2.03, Madison, WI. 2001; BRUKER Analytical X-ray Systems.

(32) Sheldrick, G. M. Crystal structure refinement with *SHELXL*. *Acta Crystallographica Section C* **2015**, *71*, 3–8.

(33) Frisch, M. J.; Trucks, G. W.; Schlegel, H. B.; Scuseria, G. E.; Robb, M. A.; Cheeseman, J. R.; Scalmani, G.; Barone, V.; Petersson, G. A.; Nakatsuji, H.; Li, X.; Caricato, M.; Marenich, A. V.; Bloino, J.; Janesko, B. G.; Gomperts, R.; Mennucci, B.; Hratchian, H. P.; Ortiz, J. V.; Izmaylov, A. F.; Sonnenberg, J. L.; Williams-Young, D.; Ding, F.; Lipparini, F.; Egidi, F.; Goings, J.; Peng, B.; Petrone, A.; Henderson, T.; Ranasinghe, D.; Zakrzewski, V. G.; Gao, J.; Rega, N.; Zheng, G.; Liang, W.; Hada, M.; Ehara, M.; Toyota, K.; Fukuda, R.; Hasegawa, J.; Ishida, M.; Nakajima, T.; Honda, Y.; Kitao, O.; Nakai, H.; Vreven, T.; Throssell, K.; Montgomery, J. A., Jr.; Peralta, J. E.; Ogliaro, F.; Bearpark, M. J.; Heyd, J. J.; Brothers, E. N.; Kudin, K. N.; Staroverov, V. N.; Keith, T. A.; Kobayashi, R.; Normand, J.; Raghavachari, K.; Rendell, A. P.; Burant, J. C.; Iyengar, S. S.; Tomasi, J.; Cossi, M.; Millam, J. M.; Klene, M.; Adamo, C.; Cammi, R.; Ochterski, J. W.; Martin, R. L.; Morokuma, K.; Farkas, O.; Foresman, J. B.; Fox, D. J. Gaussian 09, Revision D.01. **2013**, Gaussian Inc. Wallingford CT.

(34) Becke, A. D. Density-functional thermochemistry. III. The role of exact exchange. *The Journal of Chemical Physics* **1993**, *98*, 5648–5652.

(35) Küchle, W.; Dolg, M.; Stoll, H.; Preuss, H. Ab initio pseudopotentials for Hg through Rn: I. Parameter sets and atomic calculations. *Molecular Physics* **1991**, *74*, 1245–1263.

(36) Hariharan, P.; Pople, J. The influence of polarization functions on molecular orbital hydrogenation energies. *Theor. Chim. Acta* **1973**, 213–222.

(37) Ehrlich, S.; Moellmann, J.; Reckien, W.; Bredow, T.; Grimme, S. System-Dependent Dispersion Coefficients for the DFT-D3 Treatment of Adsorption Processes on Ionic Surfaces. *ChemPhysChem* **2011**, *12*, 3414–3420.

(38) Chemcraft, version 1.8 (build 568b). 2020; `https://www.chemcraftprog.com`, graphical software for visualization of quantum chemistry computations.

(39) Aquilante, F.; Autschbach, J.; Carlson, R. K.; Chibotaru, L. F.; Delcey, M. G.; De Vico, L.; Fdez. Galván, I.; Ferré, N.; Frutos, L. M.; Gagliardi, L.; Garavelli, M.; Giussani, A.; Hoyer, C. E.; Li Manni, G.; Lischka, H.; Ma, D.; Malmqvist, P. k.; Müller, T.; Nenov, A.; Olivucci, M.; Pedersen, T. B.; Peng, D.; Plasser, F.; Pritchard, B.; Reiher, M.; Rivalta, I.; Schapiro, I.; Segarra-Martí, J.; Stenrup, M.; Truhlar, D. G.; Ungur, L.; Valentini, A.; Vancoillie, S.; Veryazov, V.; Vysotskiy, V. P.; Weingart, O.; Zapata, F.; Lindh, R. Molcas 8: New capabilities for multiconfigurational quantum chemical calculations across the periodic table. *J. Comput. Chem.* **2016**, *37*, 506–541.

(40) Roos, B. O.; Taylor, P. R.; Sigbahn, P. E. A complete active space SCF method (CASSCF) using a density matrix formulated super-CI approach. *Chem. Phys.* **1980**, *48*, 157–173.

(41) Sharkas, K.; Pritchard, B.; Autschbach, J. Effects from Spin–Orbit Coupling on Electron–Nucleus Hyperfine Coupling Calculated at the Restricted Active Space Level for Kramers Doublets. *J. Chem. Theory Comput.* **2015**, *11*, 538–549, PMID: 26580911.

(42) Andersson, K.; Malmqvist, P. A.; Roos, B. O.; Sadlej, A. J.; Wolinski, K. Second-order perturbation theory with a CASSCF reference function. *J. Phys. Chem.* **1990**, *94*, 5483–5488.

(43) Sauri, V.; Serrano-Andrés, L.; Shahi, A. R. M.; Gagliardi, L.; Vancoillie, S.; Pierloot, K. Multiconfigurational Second-Order Perturbation Theory Restricted Active Space (RASPT2) Method for Electronic Excited States: A Benchmark Study. *J. Chem. Theory Comput.* **2011**, *7*, 153–168, PMID: 26606229.

(44) Roos, B. O.; Lindh, R.; Malmqvist, P.-k.; Veryazov, V.; Widmark, P.-O. Main Group Atoms and Dimers Studied with a New Relativistic ANO Basis Set. *J. Phys. Chem. A* **2004**, *108*, 2851–2858.

(45) Roos, B. O.; Lindh, R.; Malmqvist, P.-k.; Veryazov, V.; Widmark, P.-O. New Relativistic ANO Basis Sets for Transition Metal Atoms. *J. Phys. Chem. A* **2005**, *109*, 6575–6579, PMID: 16834004.

(46) Douglas, M.; Kroll, N. M. Quantum electrodynamical corrections to the fine structure of helium. *Ann. Phys.* **1974**, *82*, 89–155.

(47) Hess, B. A. Relativistic electronic-structure calculations employing a two-component no-pair formalism with external-field projection operators. *Phys. Rev. A* **1986**, *33*, 3742–3748.

(48) Heß, B. A.; Marian, C. M.; Wahlgren, U.; Gropen, O. A mean-field spin-orbit method applicable to correlated wavefunctions. *Chem. Phys. Lett.* **1996**, *251*, 365–371.

(49) Bolvin, H. An Alternative Approach to the g-Matrix: Theory and Applications. *ChemPhysChem.* **2006**, *7*, 1575–1589.

(50) Vancoillie, S.; Rulísek, L.; Neese, F.; Pierloot, K. Theoretical description of the structure and magnetic properties of nitroxide-Cu(II)-nitroxide spin triads by means of mul-

ticonfigurational ab initio calculations. *The journal of physical chemistry. A* **2009**, *113*, 6149—6157.